Concrete-filled and bare 6082-T6 aluminium alloy tubes under in-plane bending: Experiments, finite element analysis and design recommendations

Shafayat Bin Ali[a,1], **George S. Kamaris**[a], **Michaela Gkantou**[a] **and Kunal D. Kansara**[a]

[a] School of Civil Engineering and Built Environment, Liverpool John Moores University, United Kingdom

ABSTRACT

The application of aluminium alloys in structural engineering is growing owing to their high strength-to-weight ratio, aesthetic appearance and excellent resistance to corrosion. However, the low modulus of elasticity of aluminium poses adverse effects on the flexural response of structural members made of aluminium alloys. In case of tubular members, the performance can be improved with the addition of concrete infill. Research on the flexural response of concrete-filled aluminium alloy tubes is still minimal. This study presents experimental and numerical investigations on the behaviour of concrete-filled and bare 6082-T6 aluminium alloy tubular members under in-plane bending. In total 20 beams, including 10 concrete-filled aluminium alloy tubular (CFAT) and 10 bare aluminium alloy tubular (BAT) specimens, were tested. The specimens comprised of square and rectangular hollow sections and were filled with 25 MPa nominal cylinder compressive strength concrete. The experimental results are reported in terms of failure mode, flexural strength, flexural stiffness, ductility and bending moment versus mid-span deflection curve. Compared to the BAT specimens, the counterpart CFAT specimens have shown remarkably improved flexural strength, stiffness and ductility due to the concrete infill and the improvement is more pronounced for the sections with thinner sections. Finite element models of BAT and CFAT beams were developed by taking into account the nonlinearities in geometry and material and validated against the experimental data. A parametric study considering a broad range of cross-sections and different concrete grades was conducted based on the validated models. The FE results have shown that the flexural strength of the BAT and CFAT members increases with the increase of cross-sectional aspect ratio, wall thickness and concrete grade. The results obtained from experiments and numerical analysis for BAT members were used to assess the flexural capacity predictions and the

---

[1] Corresponding author: Shafayat Bin Ali
Email: S.B.Ali@2019.ljmu.ac.uk

applicability of the slenderness limits provided in the European standards. It was demonstrated that the slenderness limits provided by Eurocode 9 are conservative for Class A aluminium sections. Hence, revised Class 1, Class 2 and Class 3 limits are proposed which appear to be better applicable to Class A aluminium alloys. In the absence of design specifications for CFAT flexural members, the design rules for concrete-filled steel tubular flexural members provided by Eurocode 4 were adopted and the material properties of steel were replaced with those of aluminium alloy. It was shown that the proposed design methodology is suitable for the design of CFAT flexural members. Moreover, a slenderness limit for compact sections of CFAT flexural members is proposed based on Eurocode 4 framework.

Keywords: 6082-T6 aluminium alloy, Concrete-filled sections, Bare sections, Simply supported beams, Flexural response, Finite Element analysis

1 Introduction

Concrete-filled steel tubular (CFST) structural members have gained popularity in modern construction because of their high strength, fire resistance, elimination of temporary formwork during construction and maintenance efficiency. Replacing steel tubes with aluminium in such composite structural members can further improve their advantages due to aluminium’s low mass density, high strength-to-weight ratio, attractive appearance, excellent resistance to corrosion and ease of production [1-3]. Because of low modulus of elasticity of aluminium, stability poses concern for structural members made of aluminium alloy [4-6]. However, a concrete-filled aluminium alloy tubular (CFAT) structural member benefits from both materials, i.e., the compressive strength of concrete increases by the confinement provided by the hollow aluminium section and the inward buckling of aluminium section is prevented by the concrete infill [7-9]. This also improves the stability performance compared to the bare aluminium alloy tubular (BAT) members.

Extensive research was carried out to study the behaviour of CFST beams. Furlong [10] and Lu and Kennedy [11] experimentally investigated the response of circular CFST beams and demonstrated that the flexural strength of CFST sections substantially increased compared to their bare counterpart. Han [12] performed flexural tests on rectangular and square CFST of CFST beams. Based on a series of tests, Lu et al. [13] demonstrated that the flexural strength of CFST beams with non-uniform wall thickness is higher than the conventional CFST beams with constant wall thickness. Montuori and Piluso [14] experimentally evaluated the behaviour of CFST members under non-uniform bending moment and suggested a fibre model to determine the bending capacity of CFST members. Hou et al. [15] studied the flexural response of CFST members under sustained load and chloride corrosion and observed that the flexural capacity and ductility of CFST members deteriorated noticeably due to the chloride corrosion. A series of tests on square, rectangular and circular concrete-filled stainless-steel tubular members under in-plane bending were performed by Chen et al. [16, 17] who compared the experimental initial and serviceability limit state flexural stiffness with the design stiffness determined using American, European, British and Japanese specifications. They demonstrated that the design specifications are conservative in predicting both the initial and the serviceability limit state flexural stiffness. Zhang et al. [18] experimentally and numerically investigated the structural behaviour of CFST flexural members with elliptical sections. They also proposed design formulas that can accurately predict moment capacity and flexural stiffness of the elliptical CFST members.

A number of studies were performed to investigate the response of bare aluminium alloy flexural members. Moen et al. [19, 20] experimentally and numerically investigated the rotation capacity and strength of aluminium alloy flexural members with welded stiffeners. The specimens were manufactured by 6082 and 7108 aluminium alloys. It was shown that due to premature tensile failure the welded aluminium alloy flexural members suffered a severe loss of rotation capacity. Zhu and Young [21] conducted research on 6061-T6 aluminium alloy members subjected to pure in-plane bending and proposed design formulas for square hollow section (SHS) beams on the basis of the direct strength method. It was demonstrated that the modified direct strength method could accurately predict the bending capacity of SHS aluminium alloy beams. Su et al. [22] experimentally and numerically studied the strength of simply supported flexural members fabricated by 6061-T6 and 6063-T5 grade aluminium alloys. The experimental and numerical flexural strength were compared with the strength calculated by Australian/New Zealand, American and European standards and it was observed that the designs standards are conservative. Feng et al. [23] experimentally investigated the response of rectangular hollow section and SHS beams with circular perforations manufactured by 6061-T6 and 6063-T5 grade aluminium alloys and compared the experimental strengths with the strengths predicted using current design standards. It was shown that the North American standards for perforated steel are appropriate for perforated aluminium alloy flexural members. However, only a few experimental studies were performed to investigate the response of CFAT beams. Feng et al. [24] investigated the behaviour of square and rectangular CFAT beams and Chen et al. [25] examined the response of circular CFAT members under to in-plane bending. The authors used the 5083 non-heat-treated aluminium alloy to fabricate the specimens and concluded that the flexural strength was enhanced due to concrete infill.

Past research has mainly focused on the flexural response of CFST members, while research on CFAT members under in-plane bending is still minimal. Moreover, only few studies have focused on the response of 6082-T6 aluminium alloy flexural members. The 6082 aluminium alloy is gaining popularity in structural applications [3, 26] due to its good corrosion resistance, high strength and weldability and thus more research on its behaviour is necessary. This paper contributes to bridging this gap of knowledge by presenting experimental and numerical investigations on the flexural behaviour of CFAT and BAT members made of 6082-T6 grade alloy. The results obtained from the experiments and finite element (FE) analyses were used to assess the flexural capacity predictions and the applicability of the slenderness limits provided by Eurocode 9 (EC9) [27]. In the absence of design specifications for CFAT flexural members, the design rules for CFST flexural members provided by Eurocode 4 (EC4) [28] were adopted by replacing steel’s material properties with those of aluminium alloy.

2 Experimental investigation

2.1 Test specimens

In total 20 beams, including 10 CFAT and 10 BAT specimens with square and rectangular sections, were tested under pure in-plane bending. The aluminium sections were made of 6082-T6 grade alloy. The hollow tubes consist of different cross-sections, with nominal outer width (*B*) varied from 25.4 to 76.2 mm, nominal outer height (*H*) varied from 76.2 to 101.6 mm and nominal thickness (*t*) varied from 1.6 to 6.4 mm (Figure 1). All beams were 1000 mm long and the span (*L*) between the pinned supports was 900 mm. Table 1 provides the measured dimensions of all test specimens. The specimens are labelled based on the dimensions of their cross-section and the existence or absence of the concrete infill. For example, the designation ‘76.2×25.4×3.3’ denotes a specimen with a nominal outer height, width and thickness of 76.2 mm, 25.4 mm and 3.3 mm, respectively. The symbol ‘-C’ denotes that the specimen is CFAT, i.e., it has concrete infill, and the absence of ‘-C’ indicates that it is a BAT specimen.

CFAT specimens were prepared by filling the hollow tubes with concrete. The concrete was filled in layers and compacted using a vibrating table. Before casting, the lower end of each specimen was closed by a wooden plate and sealed with tape to prevent leakage of concrete. After casting, all beams were wrapped with a plastic membrane for a 28-days curing to avoid moisture evaporation.

The initial local geometric imperfection (ω_l) of a thin-walled plate element can influence the flexural response of the CFAT and BAT beams. Hence, the initial local geometric imperfection of all specimens was measured before the experiment and their magnitudes were considered in the FE analysis presented in Section 4. A linear height gauge was used to measure the deviation from a flat surface at 25 mm intervals along the centreline of the longitudinal direction of all sides of each specimen. The maximum value recorded was considered as the amplitude of local imperfection of the beam. The calculated values of ω_l of all specimens are presented in Table 1.

Table 1: Geometric dimensions and initial local geometric imperfections of test specimens.

Specimen	H (mm)	B (mm)	t (mm)	H/B	B/t	L (mm)	ω_l (mm)
76.2×76.2×1.6	76.3	76.2	1.54	1.00	49.48	900	0.36 (t/4)
76.2×76.2×1.6-C	76.3	76.2	1.54		49.48	900	0.55 (t/3)
76.2×76.2×3.3	76.2	76.2	3.21	1.00	23.74	900	0.12 (t/26)
76.2×76.2×3.3-C	76.2	76.2	3.21		23.74	900	1.15 (t/27)
76.2×76.2×4.8	76.2	76.1	4.71	1.00	16.16	900	0.20 (t/23)
76.2×76.2×4.8-C	76.2	76.1	4.71		16.16	900	0.71 (t/6)
76.2×76.2×6.4	76.2	76.2	6.21	1.00	12.27	900	0.26 (t/24)
76.2×76.2×6.4-C	76.2	76.2	6.21		12.27	900	0.12 (t/53)
76.2×25.4×3.3	76.3	25.5	3.33	2.99	7.66	900	0.11 (t/32)
76.2×25.4×3.3-C	76.3	25.5	3.32		7.68	900	0.65 (t/5)
76.2×38.1×3.3	76.2	38.3	3.26	1.99	11.75	900	0.10 (t/33)
76.2×38.1×3.3-C	76.2	38.3	3.26		11.75	900	0.40 (t/8)
76.2×50.8×3.3	76.1	50.7	3.15	1.50	16.10	900	0.14 (t/23)
76.2×50.8×3.3-C	76.1	50.7	3.15		16.10	900	0.52 (t/6)
101.6×25.4×3.3	101.6	25.4	3.21	4.00	7.91	900	0.31 (t/10)
101.6×25.4×3.3-C	101.6	25.4	3.20		7.94	900	0.20 (t/16)
101.6×50.8×3.3	101.9	51.4	3.44	1.98	14.94	900	0.32 (t/11)
101.6×50.8×3.3-C	101.9	51.4	3.41		15.07	900	0.16 (t/21)
101.6×76.2×3.3	101.5	76.3	3.14	1.33	24.30	900	0.28 (t/11)
101.6×76.2×3.3-C	101.5	76.3	3.14		24.30	900	0.17 (t/18)

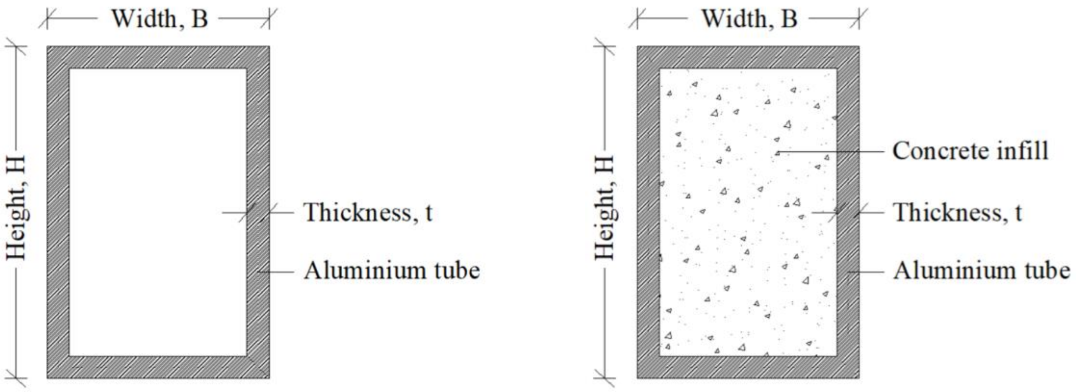

(a) (b)

Figure 1: Geometry of a typical (a) BAT section and (b) CFAT section.

2.2 Material properties

2.2.1 Aluminium tube

The mechanical properties of the aluminium alloy were obtained from tensile coupon tests. Two coupons with 12 mm width and 100 mm gauge length were prepared from each hollow tube and tested according to the recommendation of BS EN ISO 6892-1 [29]. During the test, the displacement-controlled load was employed at a rate of 0.2 mm/min and an extensometer was instrumented to obtain the data of longitudinal strains (Figure 2(a)). Equations (1) and (2) given by Ramberg and Osgood [30] and revised by Hill [31] were applied to replicate the nonlinear stress-strain response of the tested aluminium alloy.

$$\varepsilon = \frac{f}{E} + 0.002\left(\frac{f}{f_{0.2}}\right)^{n} \tag{1}$$

$$n = \frac{ln\,2}{ln\left(\frac{f_{0.2}}{f_{0.1}}\right)} \tag{2}$$

where f is the tensile stress, ε is the strain, E is the modulus of elasticity, $f_{0.1}$ is the 0.1% proof stress, $f_{0.2}$ is the 0.2% proof stress and n is the strain hardening exponent. Table 2 reports the mechanical properties determined from the coupon tests. In the table, f_u, ε_u and ε_f denote the ultimate stress at tension, the strain that corresponds to ultimate stress and the strain at fracture, respectively. Figure 2(b) presents the experimental stress-strain curve of specimen 76.2×76.2×3 together with the curve reproduced using the Ramberg-Osgood expressions.

Table 2: Mechanical properties of aluminium alloy.

Specimen	E (GPa)	$f_{0.1}$ (MPa)	$f_{0.2}$ (MPa)	f_u (MPa)	ε_u (%) (mm/mm)	ε_f (%) (mm/mm)	n
76.2×76.2×1.6	67.9	288.4	292.9	316	6.9	8.4	44.8
76.2×76.2×3.3	66.2	295.2	299.1	321	7.5	10.5	52.8
76.2×76.2×4.8	64.7	303.7	306.1	316	6.3	9.7	88.1
76.2×76.2×6.4	69.3	290.4	295.3	326	8.8	15.3	41.4
76.2×25.4×3.3	68.9	271.8	277.9	316	8.8	14.3	31.2
76.2×38.1×3.3	68.5	270.4	276.8	315	7.8	9.3	29.6
76.2×50.8×3.3	67.5	285.9	289.5	312	7.1	9.1	55.4
101.6×25.4×3.3	63.9	234.7	242.5	290	7.6	13.2	21.2
101.6×50.8×3.3	71.6	166.9	175.1	204	7.4	12.1	14.4
101.6×76.2×3.3	72.8	303.5	306.7	320	5.6	6.9	66.1

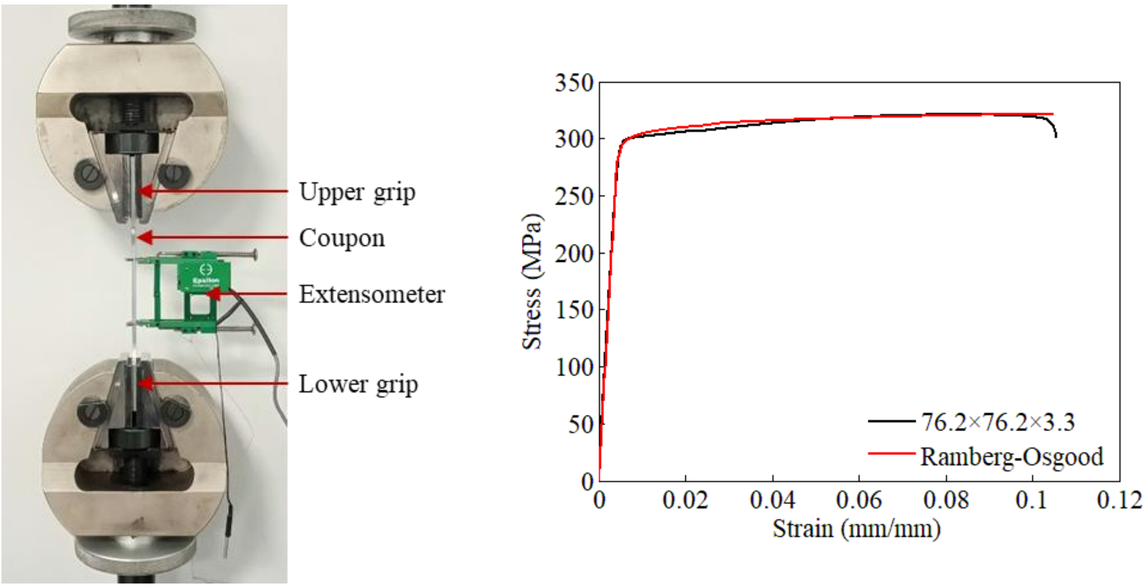

(a) (b)

Figure 2: (a) Experimental set-up of tensile coupon test, (b) Comparison of measured and Ramberg-Osgood curves of specimen 76.2×76.2×3.3.

2.2.2 Concrete

The CFAT specimens were prepared by filling concrete inside the hollow tubes. The concrete's nominal cylinder compressive strength was 25 MPa. The concrete was prepared by mixing ordinary Portland cement, sand, stone aggregates (≤ 10 mm) and water with a mixing ratio of 1:1.5:2.5:0.5 by weight. The compressive strength of concrete was determined by three compression tests of concrete cylinders and was taken as the average strength of the tests, i.e., 26.1 MPa (Table 3). The concrete cylinders with a nominal height of 300 mm and a diameter of 150 mm were prepared from the same concrete mixture used for the CFAT beams. The cylinders were tested at the test day of CFAT specimens based on the recommendation of BS EN 12390-3 [32].

Table 3: Measured material properties of concrete.

Nominal strength (MPa)	Compressive strength of cylinder (MPa)	Mean (MPa)
25	24.2 25.6 28.6	26.1

2.3 Test setup and procedure

The CFAT and BAT beams were tested under a four-point bending configuration. The span between the two pinned supports was 900 mm, while the shear span and the distance between the two loading points was 300 mm. The ratio of shear span to depth was considerably higher than 0.5 for all the specimens to prevent the shear failure of the specimens [33]. A servo-hydraulic machine with 600 kN capacity was used to apply the displacement-controlled static force with 1.5 mm/min rate. Steel rollers were used at supports, allowing rotation around the axis of bending and movement along the longitudinal direction of the specimens. The transverse compressive load was employed by two loading points at the central span of the specimens. A 20 mm thick steel plate was used at each loading point to avoid stress concentration. Moreover, wooden blocks were placed at supports and loading points inside the BAT specimens to distribute the loads along the cross-sections. Three linear variable differential transducers (LVDTs) were used to obtain the vertical deflection profile of the extreme tensile fibre of all specimens, in which one was installed at the mid-span and other two were located at the two loading points. Two strain gauges were instrumented at the outer surface of the mid-span of the top and bottom flange to record the longitudinal strain of all specimens. The readings of the strain gauges, LVDTs and applied load were recorded using a data logger. The test photograph as well as an illustrative drawing of the test set-up are presented in Figure 3.

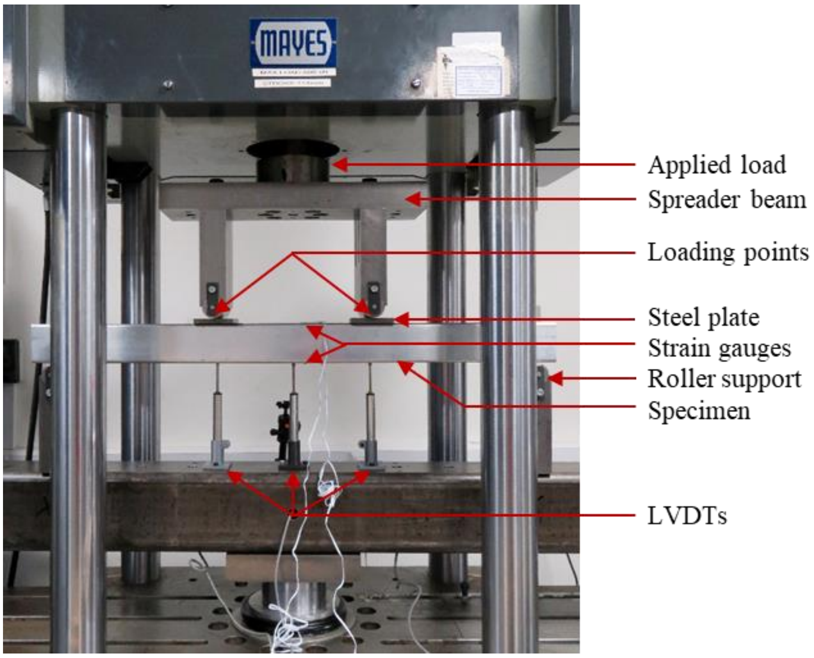

(a) Photograph

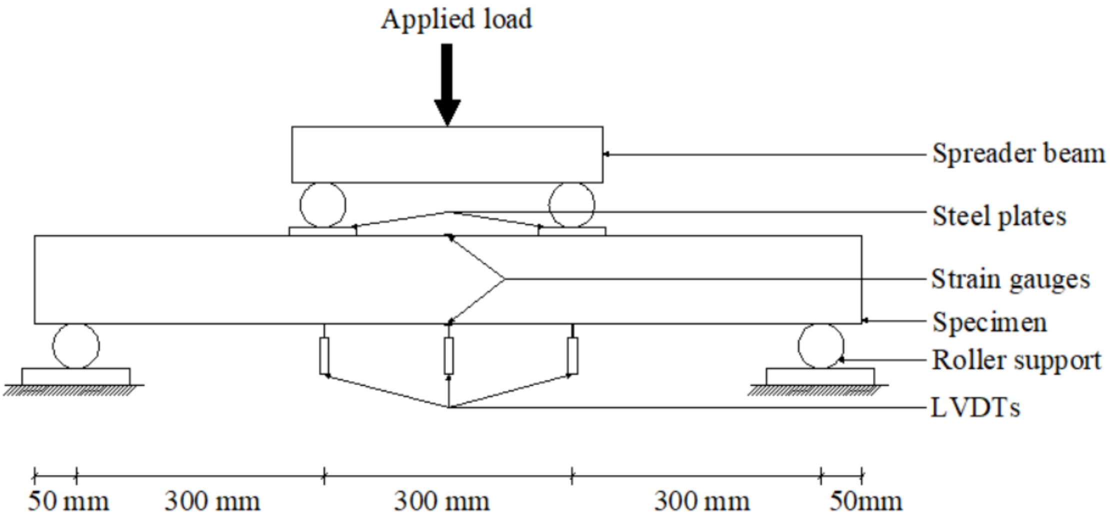

(b) Illustrative drawing

Figure 3: Test set-up and instrumentation for the four-point bending tests.

3 Test results

3.1 Failure modes

The typical modes of failure of BAT and CFAT specimens obtained from four-point bending tests are illustrated in Figure 4 and summarised in Table 4. The specimens failed by yielding (Y), local buckling (LB) or a combination of these failure modes. Figure 4(a) shows the flexural deformation of a typical specimen that failed by yielding. Most of the BAT specimens failed by yielding, except specimens 76.2×76.2×1.6, 76.2×76.2×3.3 and 101.6×76.2×3.3 which have thinner cross-section (i.e., higher *B/t* ratio) and failed by local buckling only. Besides yielding, almost all BAT specimens experienced inward and outward bulging near the loading points or the mid-span on the compression side of the specimens, including the flange and the part of the web in compression (Figure 4(b)). For all CFAT specimens, the main failure mode was yielding. In addition to yielding, local buckling was observed in the majority of the CFAT specimens whereas the inward bulging was absent and the outward bulging was smaller in comparison with the BAT specimens. This is attributed to the concrete infill that effectively restrained the development of inward buckling and delayed the outward buckling. It was observed that, in specimens which experienced combined failure modes, the flexural deformation appeared first after applying the transvers compressive load whereas the local buckling was visible later when the aluminium tube reached its yield strain. However, no local buckling was identified in BAT specimens 76.2×25.4×3.3 and 76.2×38.1×3.3 and CFAT specimens 76.2×76.2×6.4-C, 76.2×25.4×3.3-C and 76.2×38.1×3.3-C as they have thicker cross-section (i.e., lower *B/t* ratio). Moreover, in specimens 101.6×50.8×3.3, 76.2×76.2×1.6-C, 76.2×76.2×3.3-C, 101.6×50.8×3.3-C and 101.6×76.2×3.3-C, fracture was observed at the tensile zone of aluminium tube after attainment of maximum load (Figure 5(a)).

To examine the failure of infilled concrete, the aluminium alloy tubes were partly removed after the tests. Figure 5(b) shows the typical failure modes of concrete. Several parallel flexural cracks were observed between two loading points within the tension zone of concrete. These cracks were uniformly distributed and extended from tension to compression zone for the specimens failed by yielding. No diagonal cracks were observed in any specimen, indicating that shear force did not develop between the two loading points of CFAT specimens.

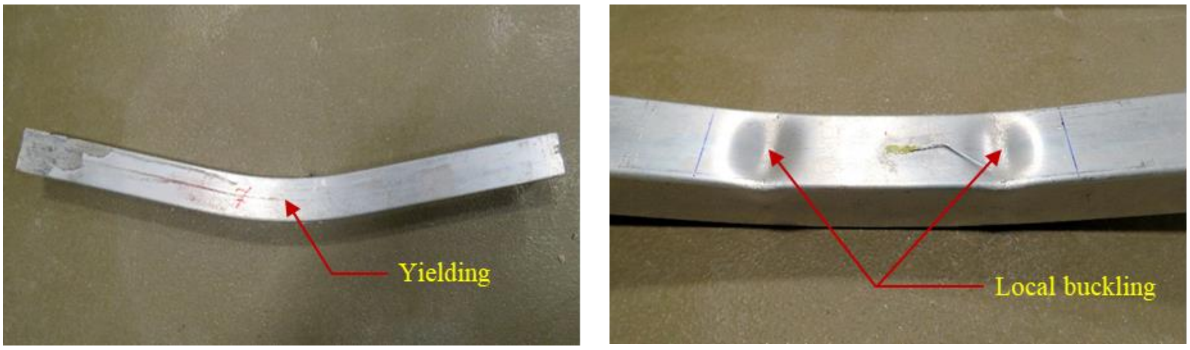

(a) 76.2×76.2×4.8-C

(b) 76.2×76.2×4.8

Figure 4: Typical failure modes: (a) Yielding, (b) Local buckling.

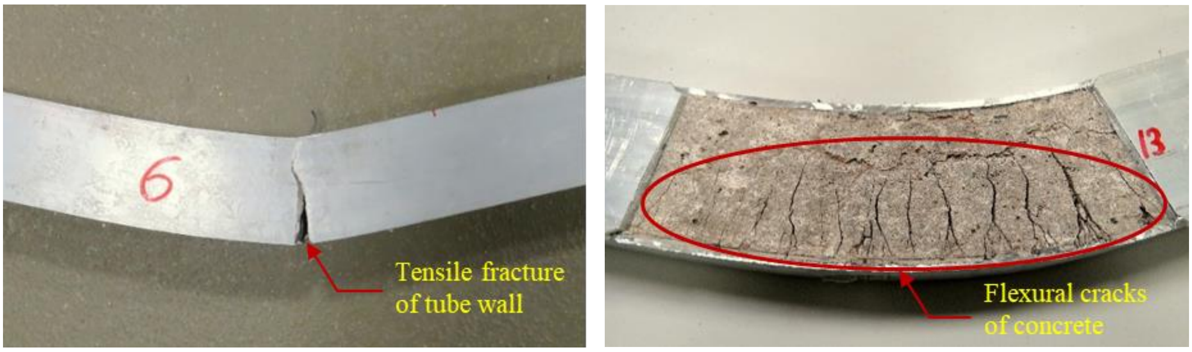

(a) 76.2×76.2×3.3-C (b) 101.6×50.8×3.3-C

Figure 5: (a) Tensile fracture of tube wall, (b) Typical failure modes of concrete.

Table 4: Observed failure modes of test specimens.

Specimen	Failure mode	Specimen	Failure mode
76.2×76.2×1.6	LB	76.2×76.2×1.6-C	Y+LB
76.2×76.2×3.3	LB	76.2×76.2×3.3-C	Y+LB
76.2×76.2×4.8	Y+LB	76.2×76.2×4.8-C	Y+LB
76.2×76.2×6.4	Y+LB	76.2×76.2×6.4-C	Y
76.2×25.4×3.3	Y	76.2×25.4×3.3-C	Y
76.2×38.1×3.3	Y	76.2×38.1×3.3-C	Y
76.2×50.8×3.3	Y+LB	76.2×50.8×3.3-C	Y+LB
101.6×25.4×3.3	Y+LB	101.6×25.4×3.3-C	Y+ LB
101.6×50.8×3.3	Y+LB	101.6×50.8×3.3-C	Y+LB
101.6×76.2×3.3	LB	101.6×76.2×3.3-C	Y+LB

Note: Y = Yielding, LB = Local buckling

3.2 Bending moment versus mid-span deflection curve

Based on the load-deformation paths recorded during the tests, bending moment versus mid-span deflection curves of BAT and CFAT flexural members are obtained and shown in Figure 6. For these plots, bending moments for the specimens are calculated using Equation (3):

$$M = \frac{PL}{6} \tag{3}$$

where P is the applied load over the specimen and L is the span. A closer look of Figure 6 reveals that, at the initial stage of the curves, the mid-span deflection increased linearly and gradually with the increase in bending moment. This linearity implies that the material of specimens was in the elastic stage. It is found that in this region the slope of the curve for the CFAT specimens is higher than that of BAT specimens, indicating an improvement of flexural stiffness due to the concrete infill. The presence of elastic-plastic region is evidenced by deviation from the initial linearity within these curves. At post-yielding, all curves of CFAT specimens and most curves of BAT specimens exhibited a fairly flat plastic plateau with steady bending moment for increasing deformation. The maximum recorded bending moment was considered as the flexural strength of the respective specimen. However, due to having good ductility~~,~~ in most of the CFAT specimens and some BAT specimens, no descending part or failure was observed at the elastic-plastic region as the post-yield plateau extended with increasing deformation. To determine the flexural strength of these specimens, a large mid-span vertical displacement limit of 60 mm (i.e., *L*/15) was adopted in this study and the bending moment recorded at this displacement was considered as the ultimate bending moment of the respective specimen. After attainment this displacement the tests were interrupted. This strategy has been applied in many recent studies [34-38] where the researchers used different mid-span vertical displacement limits to define the flexural strength of CFST beams. However, no vertical displacement limit related to CFAT beams is available in the literature as the research on CFAT flexural members is limited.

Overall, in all cases, it can be seen that due to presence of concrete infill the CFAT specimens achieved higher bending moment capacity as well as greater ductility compared to their BAT counterparts. It is also noteworthy that the BAT specimens 76.2×76.2×1.6, 76.2×76.2×3.3 and 101.6×76.2×3.3 (Figures 6(a), 6(b) and 6(j)) failed by local buckling, whereas the CFAT specimens with identical cross-section behaved in a more ductile manner.

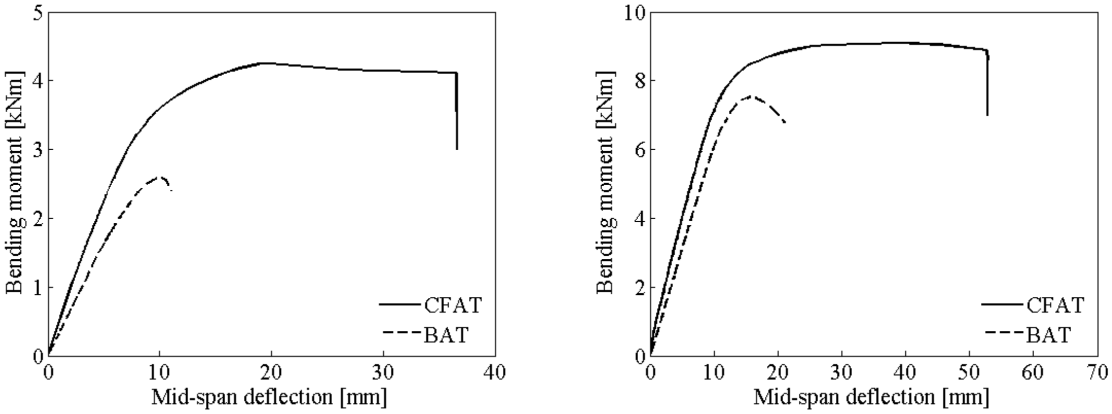

(a) 76.2×76.2×1.6 (-C)

(b) 76.2×76.2×3.3 (-C)

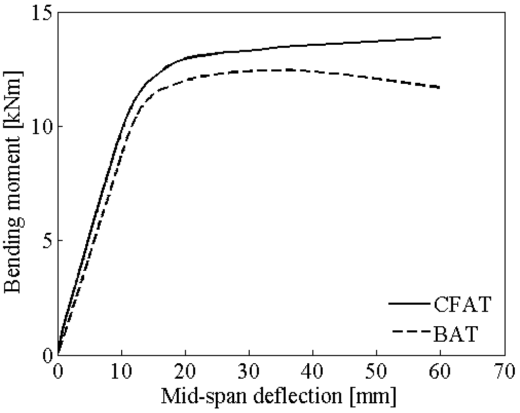

(c) 76.2×76.2×4.8 (-C)

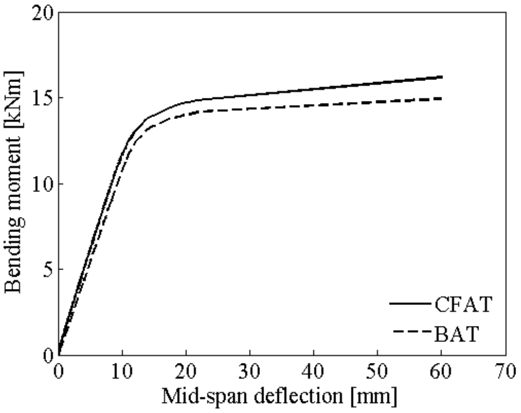

(d) 76.2×76.2×6.4 (-C)

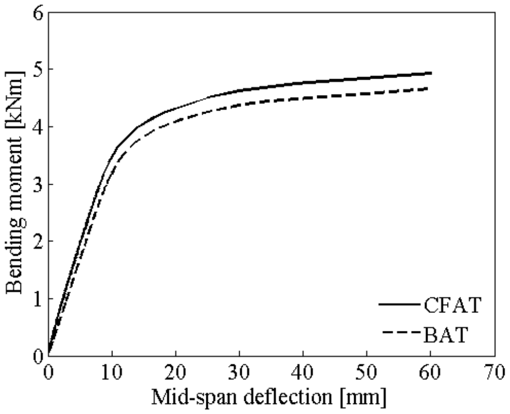

(e) 76.2×25.4×3.3 (-C)

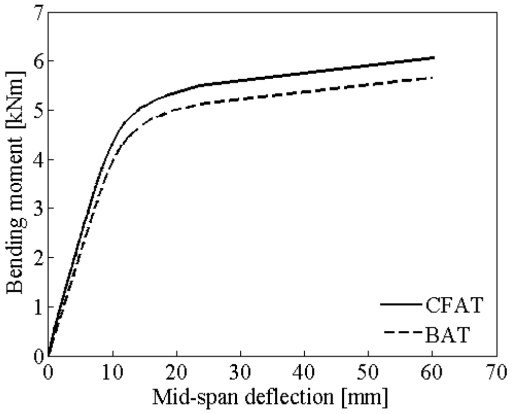

(f) 76.2×38.1×3.3 (-C)

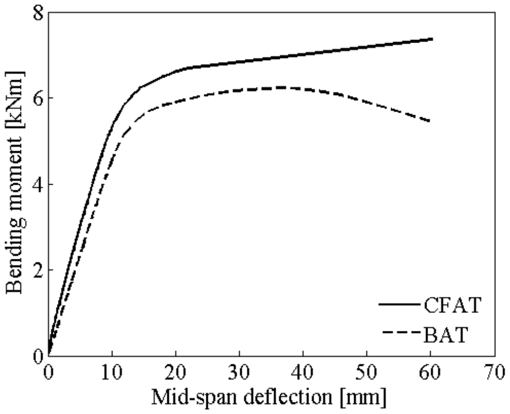

(g) 76.2×50.8×3.3 (-C)

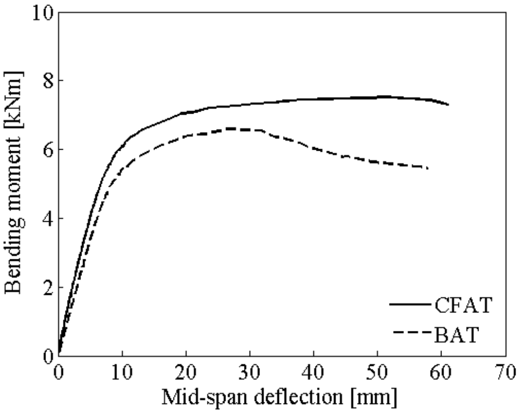

(h) 101.6×25.4×3.3 (-C)

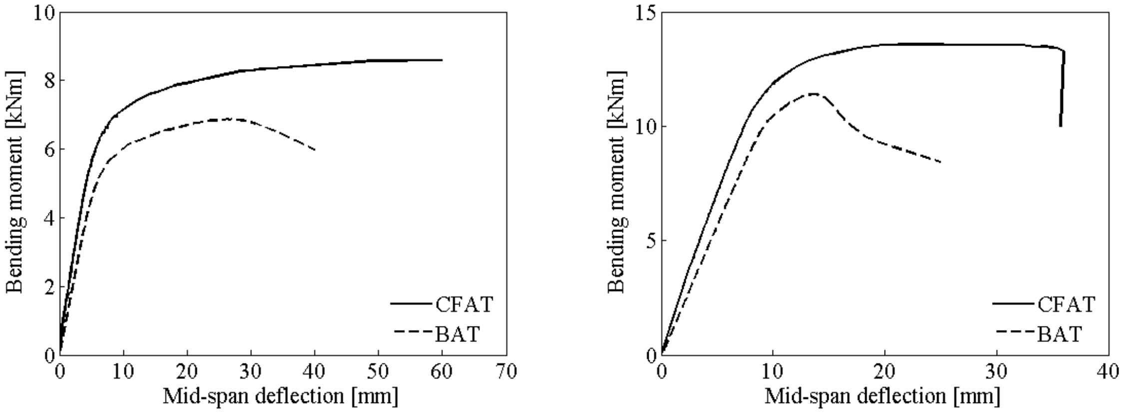

(i) 101.6×50.8×3.3 (-C)

(j) 101.6×76.2×3.3 (-C)

Figure 6: Bending moment versus mid-span deflection curves of test specimens.

3.3 Flexural strength

The ultimate bending moment recorded during testing was considered as the flexural strength of BAT and CFAT members and the obtained values are reported in Table 5. It can be seen that the flexural strengths for the square and rectangular CFAT specimens were remarkably improved due to the presence of concrete infill compared to the corresponding BAT specimens. To examine the contribution of concrete infill, the percentage increase of ultimate strength due to the concrete infill is presented in Table 5. The highest increase is noticed for specimen 76.2×76.2×1.6-C, which is equal to 64.17%. The lowest enhancement is observed for specimen 76.2×76.2×6.4-C, which is equal to 6.61%. These observations indicate that the strength enhancement increases with the decrease of the wall thickness of the cross-section. This could be attributed to the delay in the onset of local buckling in the slender plate elements offered by the concrete infill, resulting in an additional increase of the flexural strength. For the same thickness of the section, it is observed that the percentage improvement in the flexural strength is higher for members with larger width and depth. This could be related to the fact that larger aluminium cross-sections provide more confinement to concrete infill, which results in enhanced flexural strength.

Table 5: Flexural strength of test specimens.

Specimen	$M_{u,Test}$ (kNm)	$M_{u,Test}$ increase (%)
76.2×76.2×1.6	2.59	64.17%
76.2×76.2×1.6-C	4.25	
76.2×76.2×3.3	7.52	19.84%
76.2×76.2×3.3-C	9.01	

76.2×76.2×4.8	12.47	11.25%
76.2×76.2×4.8-C	13.87	
76.2×76.2×6.4	15.04	7.56%
76.2×76.2×6.4-C	16.18	
76.2×25.4×3.3	4.66	6.61%
76.2×25.4×3.3-C	4.97	
76.2×38.1×3.3	5.67	6.96%
76.2×38.1×3.3-C	6.07	
76.2×50.8×3.3	6.27	17.75%
76.2×50.8×3.3-C	7.38	
101.6×25.4×3.3	6.64	14.52%
101.6×25.4×3.3-C	7.60	
101.6×50.8×3.3	6.89	25.96%
101.6×50.8×3.3-C	8.68	
101.6×76.2×3.3	11.39	20.54%
101.6×76.2×3.3-C	13.73	

3.4 Flexural stiffness and ductility

On the basis of experimental data, the flexural stiffness and ductility of BAT and CFAT specimens have also been determined and listed in Table 6. For these calculations, the initial and serviceability limit state flexural stiffness are calculated using Equations (4) and (5) [16], respectively.

$$K_i = \frac{0.2M_u L^2}{\pi^2 \delta_i} \tag{4}$$

$$K_s = \frac{0.6M_u L^2}{\pi^2 \delta_s} \tag{5}$$

Here K_i and K_s represent the initial flexural stiffness and that at the serviceability limit state, respectively. Notations δ_i and δ_s denote the vertical displacement at the mid-span corresponding to $0.2M_u$ and $0.6M_u$, respectively.

As an indicator of the post-elastic ductility exhibited by the CFAT and BAT specimens, a ductility index μ is calculated using Equation (6) and reported in Table 6.

$$\mu = \frac{\delta_u}{\delta_y} \tag{6}$$

where δ_y represents the mid-span displacement at yield bending moment and δ_u denotes the mid-span displacement at the ultimate bending moment. It can be seen from Table 6 that the initial and serviceability limit state flexural stiffness as well as the ductility of BAT specimens increased noticeably due to the concrete infill. The increase in the flexural stiffness is more pronounced for the specimens with thinner cross-section (i.e., higher *B*/*t* ratio). However, the increase of flexural stiffness at serviceability limit state is relatively lower compared to that of initial flexural stiffness. This could be attributed to the development of cracks in concrete within the tension zone of the specimens.

Table 6: Flexural stiffness and ductility of the test specimens.

Specimen	K_i (kNm^2)	$K_{i,CFAT}$ / $K_{i,BAT}$	K_s (kNm^2)	$K_{s,CFAT}$ / $K_{s,BAT}$	δ_y (mm)	δ_u (mm)	μ	μ_{CFAT} / μ_{BAT}
76.2×76.2×1.6	29.95	55.63	26.99	33.72	4.72	10.10	2.14	48.66
76.2×76.2×1.6-C	46.61		36.09		5.80	18.45	3.18	
76.2×76.2×3.3	51.85	40.60	50.57	30.26	7.32	15.92	2.17	205.44
76.2×76.2×3.3-C	72.90		65.87		6.89	45.77	6.64	
76.2×76.2×4.8	72.50	23.79	71.37	14.41	8.60	37.53	4.36	64.39
76.2×76.2×4.8-C	89.75		81.66		8.37	60.02	7.17	
76.2×76.2×6.4	90.02	16.25	88.60	10.72	8.36	59.98	7.17	3.04
76.2×76.2×6.4-C	104.65		98.10		8.12	60.03	7.39	
76.2×25.4×3.3	28.23	22.14	27.10	11.07	8.47	60.01	7.09	4.30
76.2×25.4×3.3-C	34.48		30.10		8.13	60.08	7.39	
76.2×38.1×3.3	34.21	23.71	33.70	12.23	8.29	60.01	7.24	4.95
76.2×38.1×3.3-C	42.32		37.82		7.90	60.02	7.60	
76.2×50.8×3.3	36.87	45.49	34.14	42.38	8.14	41.67	5.12	57.25
76.2×50.8×3.3-C	53.64		48.61		7.48	60.24	8.05	
101.6×25.4×3.3	55.17	35.94	53.90	17.70	6.07	30.22	4.98	57.83
101.6×25.4×3.3-C	75.00		63.44		5.90	46.36	7.86	
101.6×50.8×3.3	77.61	47.39	76.12	25.39	4.49	27.30	6.08	120.31
101.6×50.8×3.3-C	114.39		95.45		4.48	60.01	13.40	
101.6×76.2×3.3	91.21	44.56	90.20	26.82	6.05	13.63	2.25	163.40
101.6×76.2×3.3-C	131.85		114.39		5.91	35.07	5.93	

4 Numerical investigation

The FE analysis software ABAQUS [39] was used to conduct the numerical investigation of the flexural behaviour of CFAT and BAT beams. The FE models of BAT and CFAT beams were developed accounting for the material and geometric nonlinearities. The experimental data were utilised to validate the models. A parametric study was carried out to evaluate the effect of cross-section aspect ratio, slenderness and concrete grades on the flexural response of the beams using the validated FE models.

4.1 FE modelling

FE models of all test specimens (i.e., CFAT and BAT beams) were developed based on the measured geometry and material properties of aluminium and concrete reported in Tables 1, 2 and 3, respectively. In line with past research on thin-walled tubes [36-42], four-node quadrilateral shell elements with reduced integration (S4R) were used to simulate the aluminium tubes, whereas four-node hexahedral solid elements with reduced integration (C3D8R) were adopted to model the concrete core. A mesh sensitivity study was conducted to select the reasonable element size. It was found that elements with average mesh size equal to 5 mm (L/180) provided accurate results with optimal running time. Therefore, 5 mm mesh size was assigned to both aluminium tube and concrete core using structured meshing technique. After meshing, typical BAT and CFAT beams contain over 7500 and 18500 elements, respectively.

The material properties of aluminium were considered using the elastic and plastic models provided by ABAQUS. To consider the elastic response, the values of modulus of elasticity of all aluminium tubes listed in Table 2 were utilised. To account for the plastic response, the von Mises yield criterion with isotropic hardening was used. The stress-strain data acquired from the coupon tests were inputted as true stress-strain data. The material behaviour of concrete infill was simulated using the concrete damage plasticity model provided by ABAQUS. The same model has been successfully applied in past numerical studies [7, 43, 44] of concrete-filled hollow sections. The modulus of elasticity of concrete was calculated based on EC4 [27] and the Poisson's ratio was taken as 0.2. The values of the dilation angle, the flow potential eccentricity and the viscosity parameter were considered as 40°, 0.1 and 0, respectively [45]. The ratio of the compressive strength due to biaxial loading to uniaxial compressive strength and the compressive meridian were calculated using the formula given by Papanikolaou and Kappos [46] and Yu et al. [47], respectively. The compressive stress-strain behaviour of concrete infill was considered according to the model recommended by Tao et al. [45] (Figure 7). In this model, no interaction was considered between the outer section and concrete infill up to peak compressive strength because of the variation of Poisson's ratio of the two materials. Therefore, up to ultimate strength, the stress-strain behaviour of both confined and unconfined concrete remains identical. Beyond the ultimate strength, the lateral displacement of concrete rises rapidly compared to the outer section due to the development of confining pressure between two materials. This beneficial confinement effect is considered in stress-strain response by adding a horizontal plateau and a descending branch with improved ductility. The tensile behaviour of concrete infill is considered by assuming an ascending part which is linear till 10% of concrete compressive strength [45] and a descending part which is defined by a stress-crack opening displacement relationship on the basis of fracture energy [48-50]. The compressive crushing and tensile cracking were considered as the failure modes of concrete.

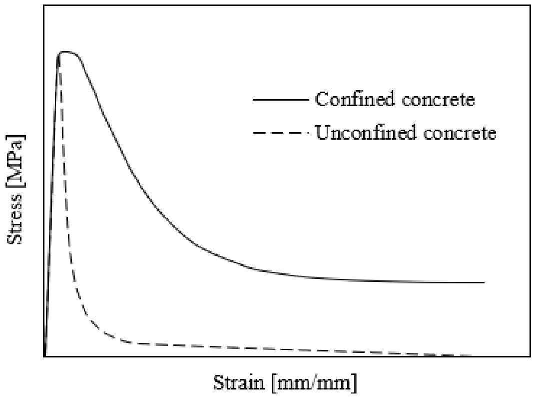

Figure 7: Confined concrete’s compressive stress-strain model [45].

The contact behaviour between the aluminium tube and the concrete infill was modelled by the surface-to-surface contact option provided by ABAQUS. A contact set was created including the inner and outer surfaces of the aluminium tube and concrete infill, respectively, where the former performed as the slave surface and the latter performed as the master surface. The hard contact model was applied in the normal direction, which allows the formation of normal stresses between two interfaces without occurring penetration during compression and separation during tension. Coulomb friction law was considered in the tangential direction with a coefficient of 0.3 to allow sliding between the two interfaces. The existence of initial local geometric imperfections of all specimens was taken into account in the FE models by defining the lowest buckling mode acquired from eigenvalue analysis. The amplitudes of initial geometric imperfection listed in Table 1 were used in the models. To replicate the boundary conditions, the rotation about the bending axis (X direction) and displacement in the axial direction of the specimen (Z direction) were left unrestrained. At loading points, the load was applied along the vertical direction (Y direction) using a displacement control approach. Figure 8 illustrates a FE model of a typical CFAT beam.

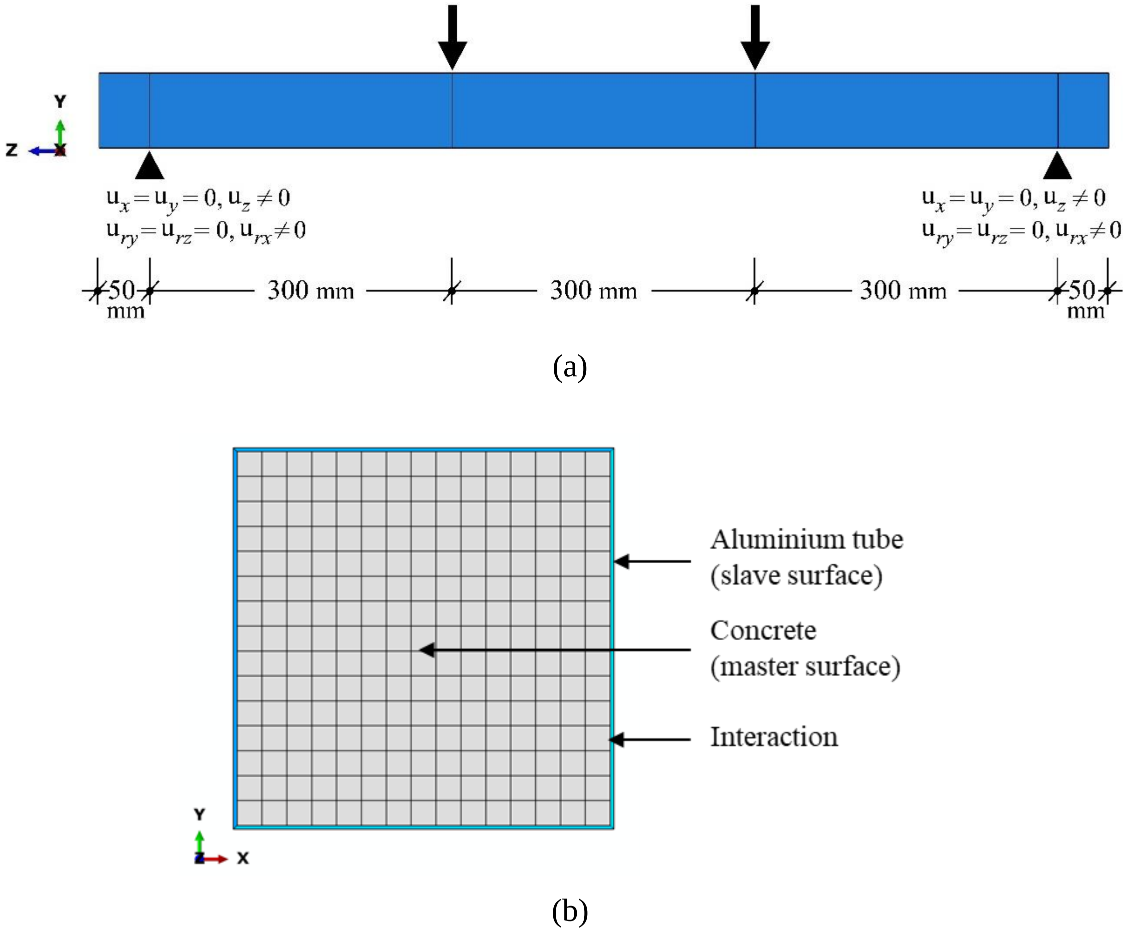

Figure 8: FE model of a typical CFAT beam: (a) geometry, loading and boundary conditions, (b) cross-section

4.2 Model validation

The precision of the developed FE models was evaluated by comparing the experimental flexural strengths, bending moment versus mid-span deflection curves and failure modes with the corresponding FE results. The ratios of the FE over the experimental flexural strength ($M_{u,FE}/M_{u,Test}$) of all specimens are reported in Table 7. Excellent agreement is noticed between the experimental data and the FE results with a mean value of the $M_{u,FE}/M_{u,Test}$ ratio equal to 0.98 and a coefficient of variation (COV) equal to 0.05. Figure 9 shows the comparison between the experimental and FE bending moment versus mid-span deflection curves of some representative specimens. It is observed that the developed FE models simulate the experimental curves very accurately. In addition, the experimental and FE failure modes of typical specimens are presented in Figure 10. It is demonstrated that the FE models fairly reproduce the deformed shapes and failure modes of the tested specimens. Overall, the developed FE models can satisfactorily predict the flexural behaviour of BAT and CFAT beams.

Table 7: Comparison of experimental and FE flexural strengths.

Specimen	$M_{u,FE}/M_{u,Test}$
76.2×76.2×1.6	1.10
76.2×76.2×1.6-C	0.96
76.2×76.2×3.3	1.01
76.2×76.2×3.3-C	1.02
76.2×76.2×4.8	0.91
76.2×76.2×4.8-C	0.94
76.2×76.2×6.4	0.95
76.2×76.2×6.4-C	0.94
76.2×25.4×3.3	0.99
76.2×25.4×3.3-C	0.98
76.2×38.1×3.3	0.98
76.2×38.1×3.3-C	0.99
76.2×50.8×3.3	0.94
76.2×50.8×3.3-C	0.92
101.6×25.4×3.3	1.05
101.6×25.4×3.3-C	1.04
101.6×50.8×3.3	0.96
101.6×50.8×3.3-C	0.94
101.6×76.2×3.3	0.94
101.6×76.2×3.3-C	0.94
Mean	0.98
COV	0.05

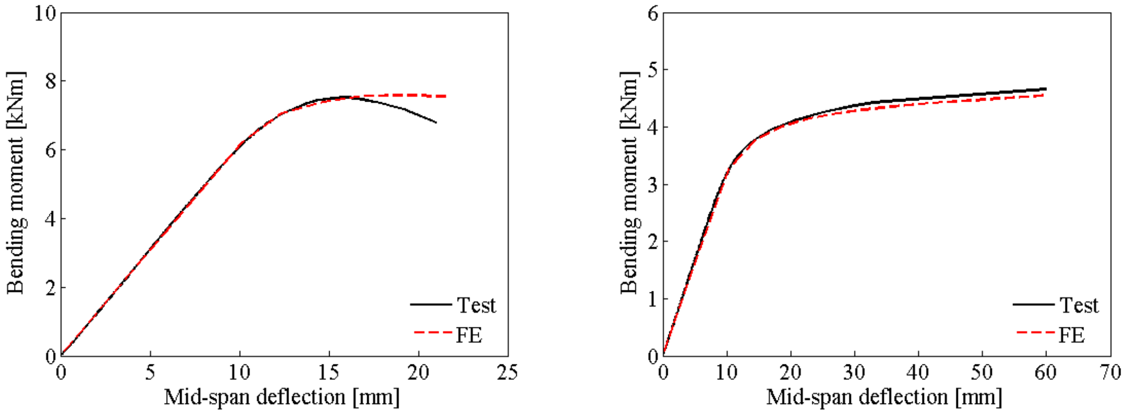

(a) 76.2×76.2×3.3

(b) 76.2×25.4×3.3

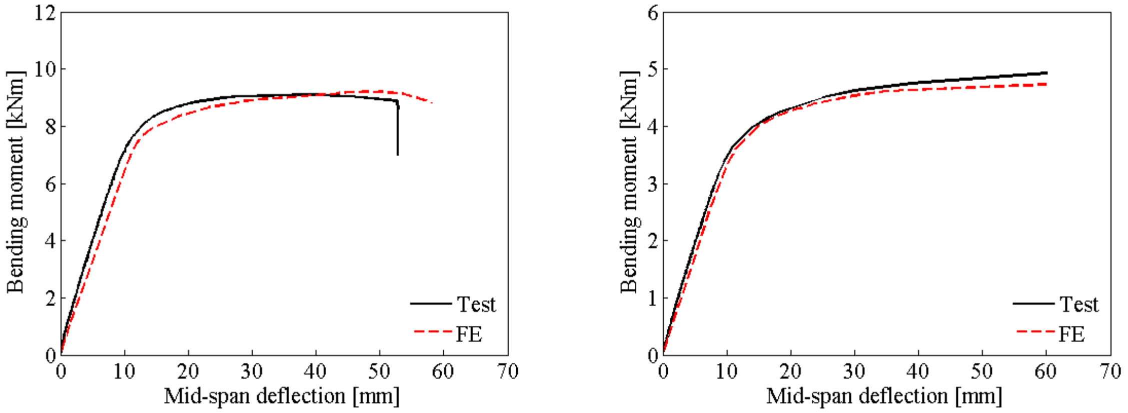

(c) 76.2×76.2×3.3 (-C)

(d) 76.2×25.4×3.3 (-C)

Figure 9: Experimental and numerical bending moment versus mid-span deflection curves.

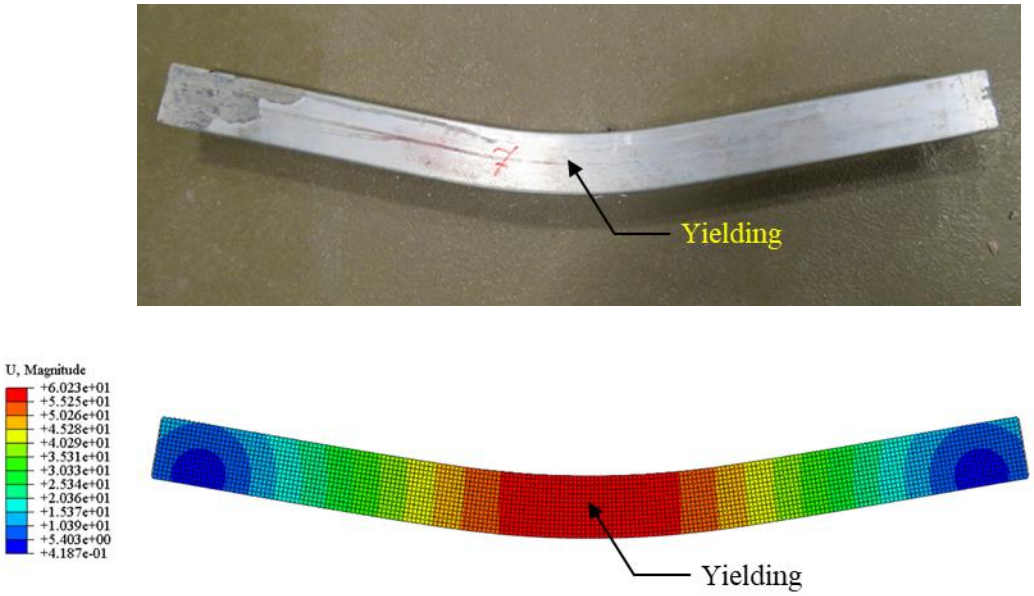

(a) 76.2×76.2×4.8 (-C)

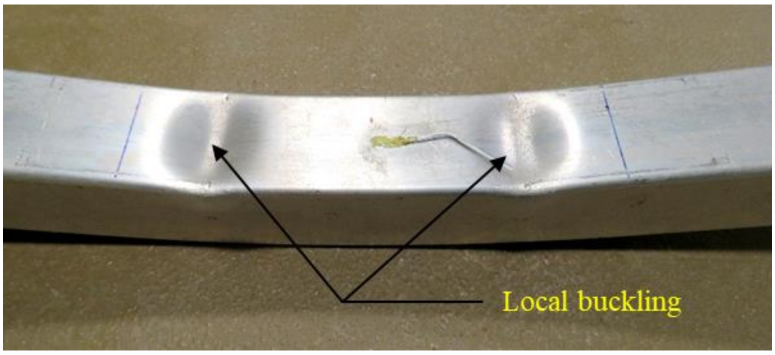

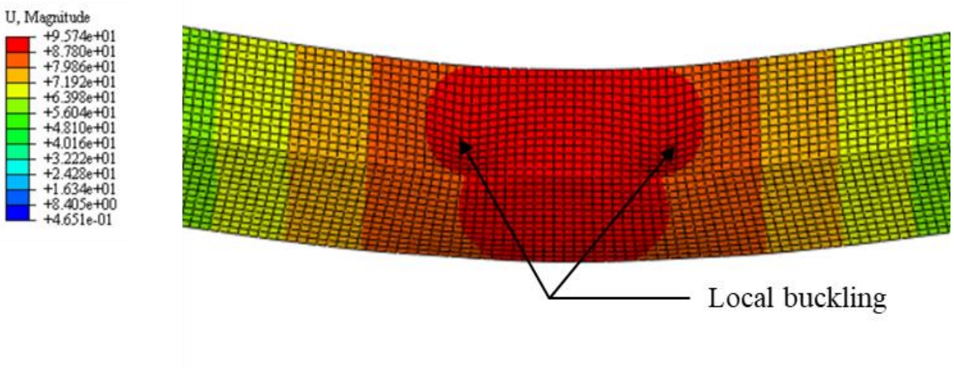

(b) 76.2×76.2×4.8

Figure 10: Experimental and FE failure modes of typical specimens.

4.3 Parametric study

A parametric study considering different cross-sections, slenderness and concrete grades was carried out based on the validated FE models. An average stress-strain curve acquired from the coupon tests was used for the aluminium tube. The average measured initial local imperfection value of $t/20$ was applied throughout. In this study, a total of 76 beams were modelled including 40 CFAT and 36 BAT specimens. Three cross-sectional aspect ratios (H/B), namely 1.0, 1.5 and 2 were considered, whilst the wall thickness was varied from 1 mm to 10 mm without changing the outer dimensions of the cross-section. Three different cylinder strengths of concrete, i.e., 30, 40 and 50 MPa were selected to study the effect of concrete grade on the behaviour of CFAT beams.

Typical results of the numerically obtained moment-deformation behaviour are presented in Figure 11. Figures 11(a) and (b) illustrate the effect of the cross-sectional aspect ratio on the bending moment versus mid-span deflection curve of square and rectangular BAT and CFAT beams, respectively. The flexural strength of the BAT and CFAT members increases with the increase of H/B when the thickness is constant. In Figures 11(c) and (d) the FE flexural response of BAT and CFAT beams with different wall thickness is illustrated, respectively, showing the higher flexural capacity for lower cross-section slenderness (i.e., largest wall thickness).

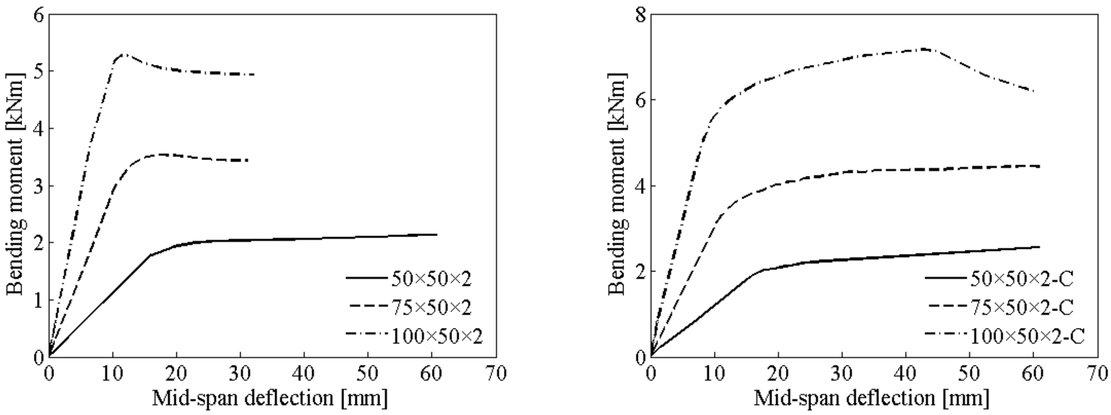

(a) BAT beams - effect of aspect ratio (b) CFAT beams - effect of aspect ratio

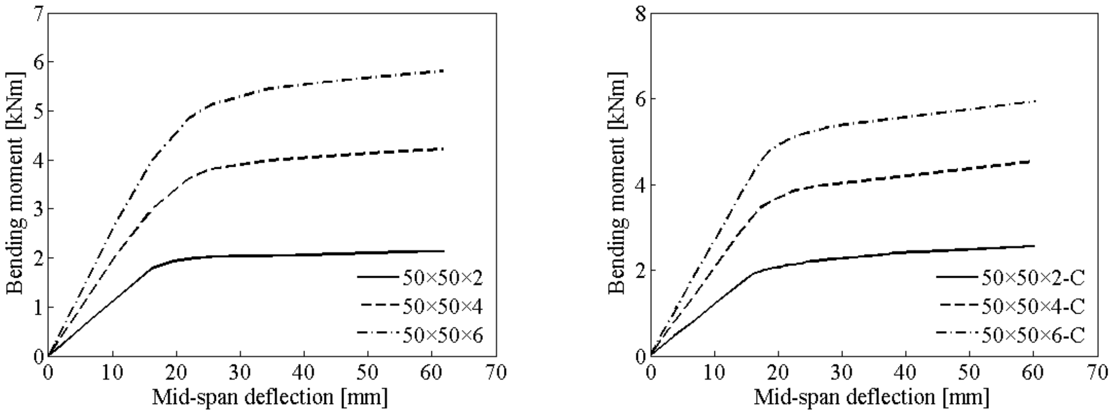

(c) BAT beams - effect of thickness (d) CFAT beams - effect of thickness

Figure 11: Typical bending moment versus mid-span deflection curves from the parametric study.

Figure 12 presents the percentage increase in flexural strength due to higher concrete grade having as reference the flexural strength of 30 MPa for typical CFAT specimens. It is found that with the increase of compressive strength of concrete the flexural strength of CFAT members enhanced up to 6.9% for 40 MPa and up to 12.6% for 50 MPa.

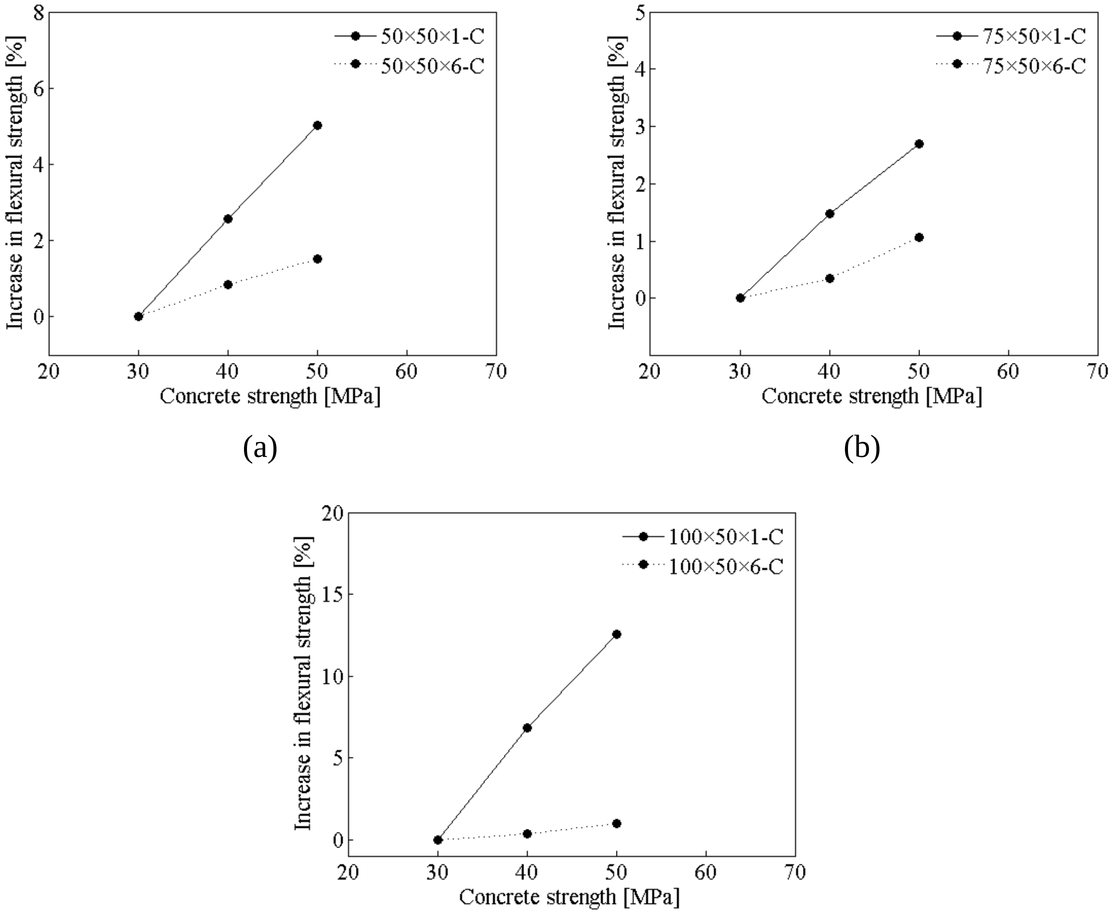

(a)

(b)

(c)

Figure 12: Effect of concrete compressive strength on the flexural strength of CFAT specimens.

5 Design Recommendations

In this section, the obtained experimental data and numerical results are used to assess the ultimate flexural capacity predictions and the applicability of the slenderness limits provided by EC9 [27] for BAT beams. Moreover, based on codified rules for CFST beams provided by EC4 [28], design recommendations are made for the flexural strength predictions and the slenderness limits for the CFAT beams. Note that the partial factors of safety were set equal to unity for the design code assessment.

5.1 Design provisions for BAT beams

5.1.1 EC9 design code

In EC9 [27], cross-sections are categorized into four classes, i.e., Class 1, 2, 3 and 4. According to EC9 [27], the design flexural capacity of a square and rectangular hollow aluminium section can be calculated by Equation (7).

$$M_{u,EC9} = \alpha_c W_{el} f_{0.2} \tag{7}$$

In the above equation, α_c is the shape factor which is defined according to the cross-section classification as follows:

$$\alpha_c = \begin{cases} W_{pl}/W_{el} & \textit{(for Class 1 \& 2)} \\ 1 & \textit{(for Class 3)} \\ W_{eff}/W_{el} & \textit{(for Class 4)} \end{cases} \tag{8}$$

where W_{el} and W_{pl} represent the elastic modulus and plastic modulus of the gross section, respectively and W_{eff} denote the effective modulus of the gross section.

5.1.2 Assessment of EC9 flexural strength prediction

The flexural strength, M_u, of BAT beams determined from experiments and FE analysis was compared with the flexural strengths calculated by EC9 [27], $M_{u,EC9}$. The moment ratios, $M_u/M_{u,EC9}$, and their corresponding mean and COV values are presented in Table 8. Figure 13 shows a comparison between flexural strength obtained from experiments and FE analysis and the corresponding predicted design strengths. Based on the above comparisons, it can be seen that EC9 [27] provides good predictions of flexural strengths with a mean value of $M_u/M_{u,EC9}$ equal to 1.06. However, the COV value reported in Table 8 indicates relatively scattered predictions.

Table 8: Comparison of experimental and FE flexural strengths with design strengths for BAT beams.

	Specimen	No	Class	$M_u/M_{u,EC9}$
Test	76.2×76.2×1.6	1	3	0.79
	76.2×76.2×3.3	1	1	0.98
	76.2×76.2×4.8	1	1	1.13

76.2×76.2×6.4	1	1	1.11	
76.2×25.4×3.3	1	1	1.17	
76.2×38.1×3.3	1	1	1.20	
76.2×50.8×3.3	1	1	1.12	
101.6×25.4×3.3	1	2	1.21	
101.6×50.8×3.3	1	1	1.14	
101.6×76.2×3.3	1	2	0.98	
FE	36	1-4	1.05	(Mean)
		Mean (all)	1.06	
		COV (all)	0.07	

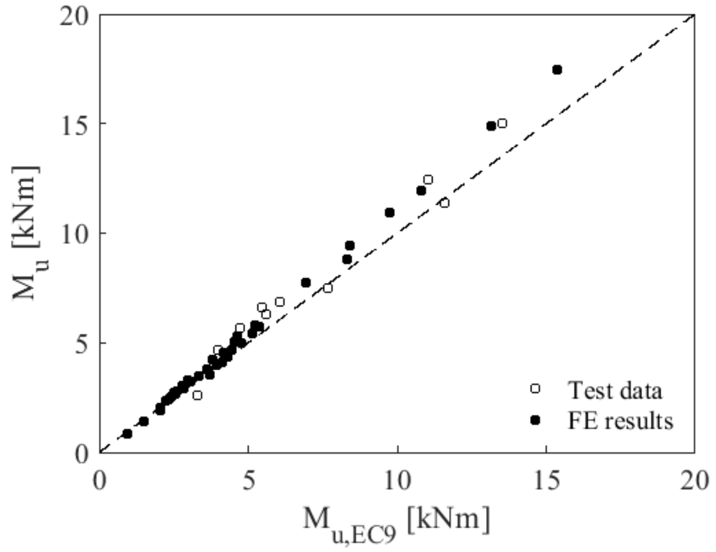

Figure 13: Comparison of test and FE flexural strengths with strengths calculated by EC9 [27] for BAT beams.

5.1.3 Assessment of EC9 Class 1 limit

According to EC9 [27], a Class 1 cross-section can achieve and sustain its full plastic moment capacity with sufficient deformation under uniaxial bending. In contrast, a Class 2 cross-section can reach full plastic capacity but cannot maintain it due to the development of inelastic local buckling. The Class 1 and Class 2 cross-sections can be distinguished based on their rotation capacity R that is defined in Equation (9) [20]:

$$R = \frac{\kappa_u}{\kappa_{pl}} - 1 \tag{9}$$

where κ_{pl} is the curvature of a beam at which the moment first reaches the plastic moment capacity, M_{pl}, and κ_u is the curvature of a beam at which the moment drops back to M_{pl} after reaching the peak flexural strength, M_u. κ_{pl} and κ_u are calculated by Equations (10) and (11), respectively.

$$\kappa_{pl} = \frac{M_{pl}}{EI} \tag{10}$$

$$\kappa_u = \frac{8(\delta - \delta_{av})}{4(\delta - \delta_{av})^2 + L_l^2} \tag{11}$$

where I is the moment of inertia of the cross-section, δ and δ_{av} are the mid-span displacement and average vertical displacement at two loading points corresponding to the moment which reaches M_{pl} again after the M_u and L_l is the distance between two loading points. For the specimens not showing any descending part in their moment-mid-span deflection curves, δ is taken as the maximum mid-span displacement δ_u. A rotation capacity of 3 is required for the plastic design of steel structures [51, 52]. In line with a past study [53], this value is considered herein for BAT flexural members.

To assess Class 1 limit for internal elements in compression of Class A materials, the rotation capacity of BAT beams obtained from the experiments and numerical analysis is plotted against the flange slenderness parameter β/ε in Figure 14. The term β is equal to b/t (where b is the flat part of the width and t is the thickness of the of the cross-section) and ε is the material factor which is equal to $\sqrt{250/f_{0.2}}$. The corresponding Class 1 slenderness limit given in EC9 [27] is shown in Figure 14 along with the rotation capacity limit of 3 [53]. It can be observed that the rotation capacities of aluminium alloy flexural members are scattered which is related to the effects of material properties as well as the interaction of constituent plates [53]. Regardless the scatteredness of data, a decreasing trend of rotation capacity with increasing member slenderness is clear. It is found that, the EC9 Class 1 limit of β/ε=11 for Class A aluminium alloy is conservative, as number of cross-sections beyond this limit satisfied the rotational capacity requirement specified in the design standard. For this reason, a new limit of β/ε=15 is proposed, which appears more suitable to categorise the Class 1 sections and is aligned with the limit suggested by Su et al. [53].

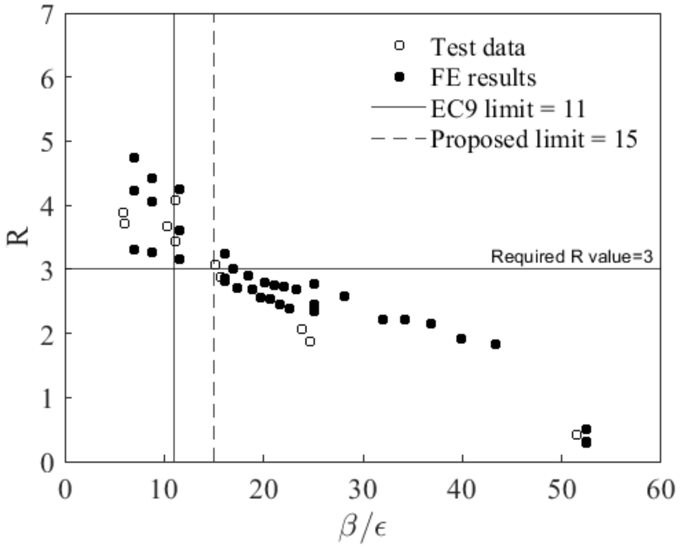

Figure 14: Assessment of Class 1 slenderness limits for internal elements of Class A materials given by EC9 [27].

5.1.4 Assessment of EC9 Class 2 limit

According to EC9 [27], the design flexural capacity of a Class 2 cross-section is the plastic moment capacity M_{pl} of the cross-section, which is the product of the plastic section modulus W_{pl} of the cross-section and the yield stress $f_{0.2}$. Hence, to assess the Class 2 limit for internal elements suggested by EC9 [27], the flexural strength M_u determined from the experiments and FE analysis is normalised by M_{pl} and plotted against the slenderness parameter β/ε of the flange in Figure 15.

An expected trend of decreasing normalised flexural strength, M_u/M_{pl}, with increasing flange slenderness can be observed in Figure 15. The horizontal line at M_u/M_{pl} equal to unity separates Class 2 (i.e., having $M_u/M_{pl} \geq 1$) from Class 3 (i.e., having $M_u/M_{pl} < 1$) cross-sections. Based on this demarcation, it can be observed from Figure 15 that the EC9 slenderness limit of $\beta/\varepsilon = 16$ appears to be strict, since many sections with values of β/ε larger than this limit have $M_u/M_{pl} \geq 1$ and can be classified as Class 2 cross-sections. Based on the experimental and numerical data of this work, a new limit of $\beta/\varepsilon = 22$ is proposed that is more appropriate as a Class 2 limit, as it includes all the sections of Figure 15 that have $M_u/M_{pl} \geq 1$.

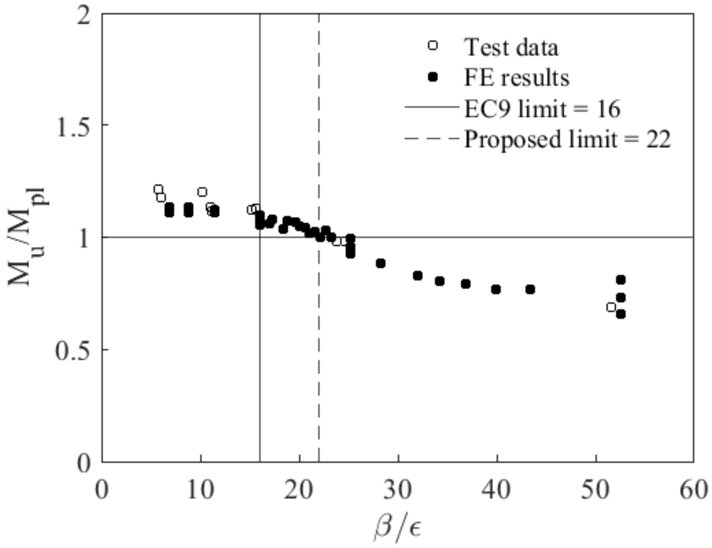

Figure 15: Assessment of Class 2 slenderness limits for internal elements of Class A materials given by EC9 [27].

5.1.5 Assessment of EC9 Class 3 limit

In EC9 [27], the cross-sections that can achieve the elastic moment capacity (i.e., moment related to the first yielding), but experience local buckling before reaching the plastic moment capacity are defined as Class 3 cross-sections. On the other hand, Class 4 sections fail by local buckling before reaching the elastic moment capacity. In Figure 16, the ultimate bending strength M_u normalised by elastic moment capacity M_{el} $(W_{el} f_{0.2})$ are plotted against flange slenderness β/ε to assess EC9 Class 3 limit for internal elements in compression. Similar to Figure 15, the horizontal line in Figure 16 at M_u/M_{el} equal to unity separates Class 3 cross-sections (i.e., having $M_u/M_{el} \geq 1$) and Class 4 cross-section (i.e., having M_u/M_{el} <1.0). It can be observed from this figure that the slenderness limit of β/ε=22 specified in EC9 is conservative for the internal elements of Class 3 aluminium sections, as some cross-sections beyond this limit achieve flexural capacity higher than the elastic moment capacity, i.e., $M_u/M_{el} \geq 1$. Thus, a Class 3 limit of β/ε=31 is suggested, as it seems to be more suitable on the basis of the experimental and numerical findings of this study.

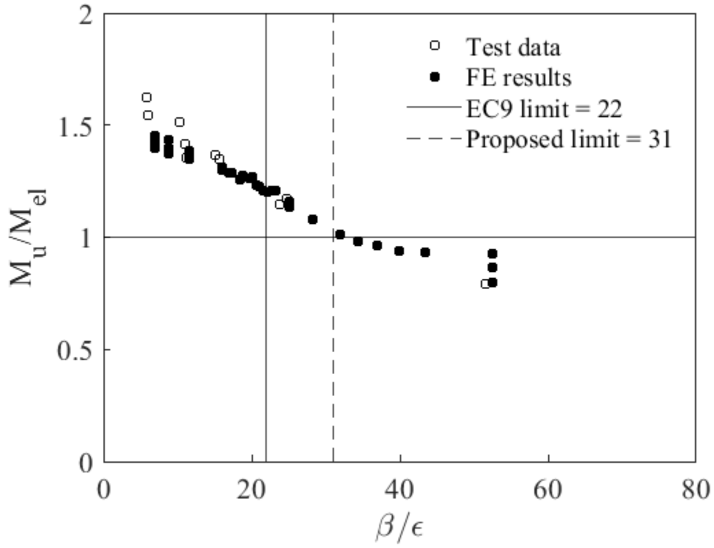

Figure 16: Assessment of Class 3 slenderness limits for internal elements of Class A materials given by EC9 [27].

5.2 Design provisions for CFAT beams

In the absence of design specifications for CFAT structural members, design recommendations for evaluating the flexural strength of CFAT beams based on codified provisions for steel-concrete composite members are discussed in this section. In particular, in Section 5.2.1, it is proposed to adopt the design methodology of EC4 [28] for CFAT beams by replacing the steel's material properties with those of aluminium alloy.

5.2.1 EC4 design methodology for CFAT beams

Based on EC4 [28], the design bending capacity of square and rectangular CFAT flexural members can be obtained using the following design formula:

$$M_{u,prop} = M_{pl} = \left(W_{pla} - W_{pla,n}\right) f_{0.2} + 0.5\left(W_{plc} - W_{plc,n}\right) f_c \tag{12}$$

where W_{pla} and W_{plc} are the plastic section moduli of the aluminium tube and concrete, respectively, which are determined by Equation (13) and (14), respectively. $W_{pla,n}$ and $W_{plc,n}$ are the plastic section moduli of the aluminium tube and concrete from $2h_n$, respectively, which are calculated by Equation (15) and (16), respectively. The term h_n is the location of the neutral axis determined by Equation (17), where A_c and f_c are the area and compressive strength of concrete, respectively. In Equation (13) and (14), r_{int} represents the internal corner radius of the hollow tube which is taken zero herein. The cross-sections of aluminium tubes of CFAT specimens are classified based on the criteria provided by EC9 [27] and the revised slenderness limits proposed in Section 5.1.

$$W_{pla} = \frac{BH^2}{4} - \frac{2}{3}\left(r_{int} + t\right)^3 - \left(r_{int} + t\right)^2 \left(4 - \pi\right)\left(\frac{H}{2} - t - r_{int}\right) - W_{plc} \tag{13}$$

$$W_{plc} = \frac{\left(B - 2t\right)\left(H - 2t\right)^2}{4} - \frac{2}{3} r_{int}{}^3 - r_{int}{}^2 \left(4 - \pi\right)\left(\frac{H}{2} - t - r_{int}\right) \tag{14}$$

$$W_{pla,n} = Bh_n{}^2 - W_{plc,n} \tag{15}$$

$$W_{plc,n} = \left(B - 2t\right) h_n{}^2 \tag{16}$$

$$h_n = \frac{A_c f_c}{2Bf_c + 4t\left(2 f_{0.2} - f_c\right)} \tag{17}$$

5.2.2 Flexural strength prediction for CFAT beams

To assess the applicability of the proposed design methodology, Table 9 presents the moment ratio of $M_u / M_{u,prop}$ along with the mean and COV values. The mean value of $M_u / M_{u,prop}$ is 1.04, indicating that design rules of EC4 [28] offer good predictions. In Figure 17, the flexural strengths obtained from tests and FE analysis are plotted against the ultimate bending moments calculated by EC4 [28]. It can be observed that the EC4 [28] are quite accurate. Overall, it can be concluded that the proposed design methodology can be applied for predicting the flexural capacity of CFAT beams.

Table 9: Comparison of test and FE flexural strengths with design strengths for CFAT beams.

	Specimen	No	Class	$M_u / M_{u,prop}$
Test	76.2×76.2×1.6-C	1	3	0.93
	76.2×76.2×3.3-C	1	1	1.06
	76.2×76.2×4.8-C	1	1	1.17
	76.2×76.2×6.4-C	1	1	1.14
	76.2×25.4×3.3-C	1	1	1.17
	76.2×38.1×3.3-C	1	1	1.18
	76.2×50.8×3.3-C	1	1	1.20
	101.6×25.4×3.3-C	1	2	1.28
	101.6×50.8×3.3-C	1	1	1.24
	101.6×76.2×3.3-C	1	2	1.04

FE	40	1-4	1.02	(Mean)
		Mean (all)	1.04	
		COV (all)	0.09	

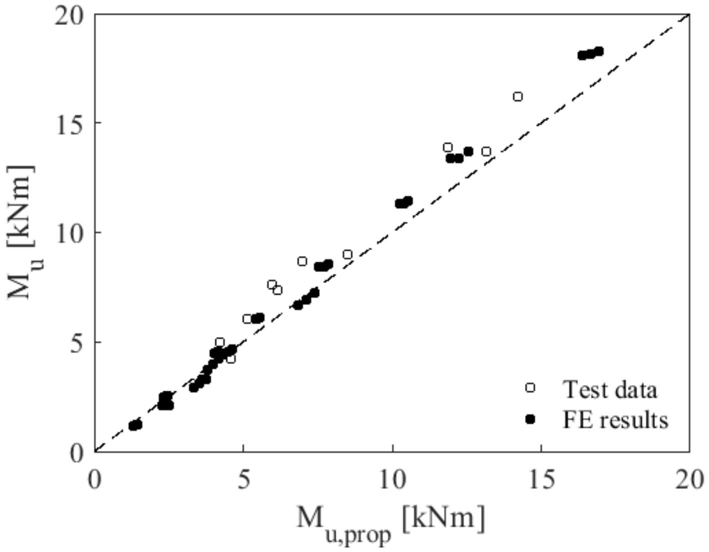

Figure 17: Comparison of test and FE flexural strengths with strengths calculated by the proposed design methodology for CFAT beams.

5.2.3 Slenderness limits for CFAT flexural members

According to EC4 [28], the effect of local buckling can be neglected for composite cross-sections if the slenderness value, β_1/ε of these sections does not exceed 52. These composite cross-sections are considered as compact sections. In β_1/ε, $\beta_1 = H/t$, H is the height of the cross-section and $\varepsilon = \sqrt{235/f_{0.2}}$. To obtain a slenderness limit for compact sections of CFAT flexural members, the moment ratio M_u/M_{pl} determined from experimental and FE results are plotted against the β_1/ε in Figure 18. Here the material factor ε for aluminium alloy is considered $\sqrt{250/f_{0.2}}$ based on EC9 [27]. Based on the data obtained in this study, the limit of β_1/ε =46 appears appropriate for the compact section of CFAT flexural members.

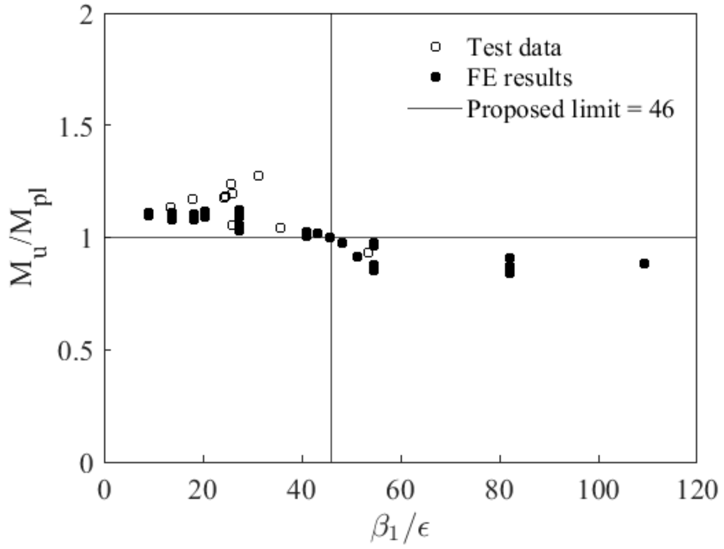

Figure 18: Proposed slenderness limits for CFAT flexural members.

6 Conclusions

This study presented experimental and numerical investigations on the performance of concrete-filled and bare 6082-T6 aluminium alloy tubular members under in-plane bending. In total 20 beams, including 10 CFAT and 10 BAT specimens, were tested. FE models of BAT and CFAT specimens were developed and used to conduct a parametric study. Based on the observed experimental and numerical results the following conclusions can be drawn:

1) The flexural strength, flexural stiffness and ductility of CFAT specimens were significantly higher than those of BAT specimens with identical cross-sections. This signifies the effectiveness of concrete infill in reducing the possibility and extent of local buckling of bare aluminium sections.
2) It was also shown that the strength increase because of the concrete infill was more prominent for slender cross-sections. This is attributed to the delay in the onset of local buckling in the slender plate elements offered by the concrete infill, resulting in an additional increase of the ultimate strength.
3) It was demonstrated that the developed FE models can accurately predict the flexural behaviour of BAT and CFAT beams. Hence, a parametric study was performed, including 76 beams (40 CFAT beams and 36 BAT beams) with broad range of cross-sections and different concrete grades.
4) The FE results have shown that the flexural strength of the BAT and CFAT members increases with the increase of *H*/*B* when the thickness is constant. Moreover, based on

the flexural response of BAT and CFAT beams with different wall thickness, it was shown that the higher flexural capacity was observed for sections with lower cross-section slenderness.

5) Based on the FE results, it was shown that with the increase of concrete compressive strength, the flexural strength of CFAT members is generally enhanced.
6) The applicability of the slenderness limits provided by EC9 were assessed based on the experimental and numerical results. It was demonstrated that the current slenderness limits in EC9 are conservative for Class A aluminium sections. Hence, revised Class 1, Class 2 and Class 3 limits are proposed which appear to be better applicable to Class A aluminium alloys.
7) In the absence of design specifications for CFAT flexural members, the design rules for CFST flexural members provided by EC4 are adopted by replacing the steel's material properties with those of aluminium alloy. It was shown that the proposed methodology can sufficiently predict the flexural strength of CFAT members.
8) A slenderness limit for compact sections of CFAT flexural members was proposed based on EC4 framework.

Acknowledgements

The authors are grateful to the technicians of the Schools of Civil Engineering and Built Environment and Engineering at Liverpool John Moores University for their valuable assistance. The financial support of Faculty of Engineering and Technology of Liverpool John Moores University is gratefully acknowledged.

References

[1] Mazzolani FM. Competing issues for aluminium alloys in structural engineering. Prog Struct Eng Mater. 2004;6(4):185–96.

[2] Georgantzia E, Gkantou M, Kamaris GS. Aluminium alloys as structural material: A review of research. Eng Struct. 2021;227:111372.

[3] Patel V, Liang Q, Hadi M. Numerical simulations of circular high strength concrete-filled aluminum tubular short columns incorporating new concrete confinement model. Thin-Walled Struct. 2020;147:106492.

[4] Mazzolani FM. Aluminium alloy structures. 2nd ed London Chapman Hall. 1995.

[5] Zhu JH, Young B. Aluminum alloy circular hollow section beam-columns. Thin-Walled Struct. 2006;44:131–40.

[6] Zhu JH, Young B. Behavior and design of aluminum alloy structural members. Adv. Steel Constr. 2008;4:158–72.

[7] Georgantzia E, Ali SB, Gkantou M, Kamaris GS, Kansara KD, Atherton W. Flexural buckling performance of concrete-filled aluminium alloy tubular columns. Eng Struct. 2021;242:112546.

[8] Ali SB, Kamaris GS, Gkantou M, Kansara KD, Hashim K. Numerical study of concrete-filled aluminium alloy tubular columns under eccentric compression. In IOP Conference Series: Materials Science and Engineering. 2021;1058:012010.

[9] Georgantzia E, Gkantou M. Flexural buckling of concrete-filled aluminium alloy CHS columns: Numerical modelling and design. Lecture Notes in Civil Engineering. 2021;143:697–707.

[10] Furlong RW. Strength of steel-encased concrete beam-columns. J Struct Div ASCE. 1967;93(ST5):113–24.

[11] Lu YQ, Kennedy DJL. The flexural behaviour of concrete-filled hollow structural sections. Can J Civ Eng. 1994;21(1):111–30.

[12] Han LH. Flexural behaviour of concrete-filled steel tubes. J Constr Steel Res. 2004;60(1–2):313–37.

[13] Lu FW, Li SP, Li DW, Sun GJ. Flexural behavior of concrete filled non-unithickness walled rectangular steel tube. J Constr Steel Res. 2007;63(8):1051–57.

[14] Montuori R, Piluso V. Analysis and modeling of CFT members: moment curvature analysis. Thin-Walled Struct. 2015;86(1):157–66.

[15] Hou CC, Han LH, Wang QL, Hou C. Flexural behavior of circular concrete filled steel tubes (CFST)under sustained load and chloride corrosion. Thin-Walled Struct. 2016;107:182–96.

[16] Chen Y, Feng R, Wang L. Flexural behaviour of concrete-filled stainless steel SHS and RHS tubes. Eng Struct. 2017;134:159–71.

[17] Chen Y, Wang K, Feng R, He K, Wang L. Flexural behaviour of concrete-filled stainless steel CHS subjected to static loading. J Constr Steel Res. 2017;139:30–43.

[18] Zhang T, Gong Y, Ding F, Liu X, Yu Z. Experimental and numerical investigation on the flexural behavior of concrete-filled elliptical steel tube (CFET). J Build Eng. 2021;41:102412.

[19] Moen LA, Langseth M, Hopperstad OS. Rotational capacity of aluminium beams under moment gradient I: experiments. J Struct Div ASCE. 1999;125(8):910–20.

[20] Moen LA, Hopperstad OS, Langseth M. Rotational capacity of aluminium beams under moment gradient II: numerical simulations. J Struct Div ASCE. 1999;125(8):921–29.

[21] Zhu JH, Young B. Design of Aluminum Alloy Flexural Members Using Direct Strength Method. J Struct Eng ASCE. 2009;135(5):558–566.

[22] Su M, Young B, Gardner L. Deformation-based design of aluminium alloy beams. Eng Struct. 2014;80:339–349.

[23] Feng R, Sun W, Shen C, Zhu J. Experimental investigation of aluminum square and rectangular beams with circular perforations. Eng Struct. 2017;151:613–632.

[24] Feng R, Chen Y, Gong W. Flexural behaviour of concrete-filled aluminium alloy thin-walled SHS and RHS tubes. Eng Struct. 2017;137:33–49.

[25] Chen Y, Feng R, Gong W. Flexural behavior of concrete-filled aluminum alloy circular hollow section tubes. Constr Build Mater. 2018;165:295–319.

[26] Kissell J, Ferry R. Aluminum structures: a guide to their specifications and design. New York John Wiley Sons. 2002.

[27] European Committee for Standardisation (EC9). Eurocode 9: Design of aluminium structures. Part 1-1: General structural rules - General structural rules and rules for buildings. BS EN 1999-1-1:2007, CEN: 2007, BSI, 2007.

[28] European Committee for Standardisation (EC4). Eurocode 4: Design of Composite Steel and Concrete Structures. Part 1-1: General Rules and Rules for Buildings. BS EN 1994-1-1: 2004, CEN: 2004, BSI, 2004.

[29] BS EN ISO 6892-1. Metallic Materials – Tensile Testing – Part 1: Method of test at room temperature. European Committee for Standardization (CEN), Brussels, 2009.

[30] Ramberg W, Osgood WR. Description of stress-strain curves by three parameters. Technical Note No. 902. Washington, D.C., USA: National Advisory Committee for Aeronautics, 1943.

[31] Hill HN. Determination of stress-strain relations from “offset” yield strength values. Technical Note No. 927; 1944.

[32] BS EN 12390-3. Testing hardened concrete. Compressive strength of test specimens. European Committee for Standardization (CEN), Brussels, 2009.

[33] Xu C, Haixiao L, Chengkui H. Experimental study on shear resistance of self-stressing concrete filled circular steel tubes. J Constr Steel Res.. 2009;65:801–07.

[34] Li G, Liu D, Yang Z, Zhang C. Flexural behavior of high strength concrete filled high strength square steel tube. J Constr Steel Res. 2017;128:732–44.

[35] Lu Y, Liu Z, Li S, Li W. Behavior of steel fibers reinforced self-stressing and self-compacting concrete-filled steel tube subjected to bending. Constr Build Mater. 2017;156:639–51.

[36] Javed MF, Sulong NHR, Memon SA, Rehman SK, Khan NB. Flexural behaviour of steel hollow sections filled with concrete that contains OPBC as coarse aggregate. J Constr Steel Res. 2018;148:287–94.

[37] Al-Shaar AAM, Göğüş MT. Flexural behavior of lightweight concrete and self-compacting concrete-filled steel tube beams. J Constr Steel Res. 2018;149:153–64.

[38] Al Zand AW, Badaruzzaman WHW, Al-Shaikhli MS, Ali MM. Flexural performance of square concrete-filled steel tube beams stiffened with V-shaped grooves. J Constr Steel Res. 2020;166:105930.

[39] Karlsson Hibbitt, Sorensen, Inc. ABAQUS. ABAQUS/Standard User’s Manual Volumes I-III and ABAQUS CAE Manual, 2016. Pawtucket (USA), Version 2016.

[40] Wang J, Afshan S, Gkantou M, Theofanous M, Baniotopoulos C, Gardner L. Flexural behaviour of hot-finished high strength steel square and rectangular hollow sections. J Constr Steel Res. 2016;121:97–109.

[41] Gkantou M, Theofanous M, Wang J, Baniotopoulos C and Gardner L. 2017. Behaviour and design of high-strength steel cross-sections under combined loading. Proceedings of the Institution of Civil Engineers-Structures and Buildings. 2017;170(11):841–854.

[42] Gkantou M. Numerical Study of Aluminium Alloy Square Hollow Section Columns. Lecture Notes in Civil Engineering. 2021;143 LNCE:709–717.

[43] Tziavos NI, Gkantou M, Theofanous M, Dirar S, Baniotopoulos C. 2020, October. Behaviour of grout-filled double-skin tubular steel stub-columns: Numerical modelling and design considerations. Struct. 2020;27:1623–1636.

[44] Gkantou M, Theofanous M, Baniotopoulos C. 2020. A numerical study of prestressed high strength steel tubular members. Front Struct Civil Eng. 2020;14(1):10–22.

[45] Tao Z, Wang ZB, Yu Q. Finite element modelling of concrete-filled steel stub columns under axial compression. J Constr Steel Res. 2013;89:121–131.

[46] Papanikolaou V, Kappos A. Confinement-sensitive plasticity constitutive model for concrete in triaxial compression. Int J of Solids Struct. 2007;44(21):7021–7048.

[47] Yu T, Teng J, Wong Y, Dong S. Finite element modeling of confined concrete-I: Drucker-Prager type plasticity model. Eng Struct. 2010;32(3):665–679.

[48] Hordijk D. Local approach to fatigue of concrete (PhD Thesis) (Delft: Delft University of Technology). 1991.

[49] FIP. Ceb-Fip Model Code 1990. Ceb-Fip Model Code 1990. 1993.

[50] Bažant Z, Becq-Giraudon E. Statistical prediction of fracture parameters of concrete and implications for choice of testing standard. Cem. Concr. Res. 2002;32:529–56.

[51] European Committee for Standardisation (EC3). Eurocode 3: Design of steel structures - Part 1-1: General rules and rules for buildings. BS EN 1993-1-1:2005, CEN: 2005, BSI, 2005.

[52] American Institute of Steel Construction (AISC). Specification for Structural Steel Buildings. ANSI/AISC 360-16, Chicago-Illinois, 2010.

[53] Su M, Young B, Gardner L. Classification of Aluminium Alloy Cross-sections. Eng Struct. 2017;141:29-40.